Published in final edited form as:
Magn Reson Med. 2013 March 1; 69(3): 793–802. doi:10.1002/mrm.24320.

High resolution human diffusion tensor imaging using 2-D navigated multi-shot SENSE EPI at 7 Tesla

Ha-Kyu Jeong[a,b], **John C. Gore**[a,b,c], and **Adam W. Anderson**[a,b,c]

[a]Vanderbilt University Institute of Imaging Science, Vanderbilt University, 1161 21st Avenue South, Nashville, Tennessee 37232, USA

[b]Department of Radiology and Radiological Sciences, Vanderbilt University, 1161 21st Avenue South, Nashville, Tennessee 37232, USA

[c]Department of Biomedical Engineering, Vanderbilt University, 1161 21st Avenue South, Nashville, Tennessee 37232, USA

Abstract

The combination of parallel imaging with partial Fourier acquisition has greatly improved the performance of diffusion-weighted single-shot EPI and is the preferred method for acquisitions at low to medium magnetic field strength such as 1.5 or 3 Tesla. Increased off-resonance effects and reduced transverse relaxation times at 7 Tesla, however, generate more significant artifacts than at lower magnetic field strength and limit data acquisition. Additional acceleration of *k*-space traversal using a multi-shot approach, which acquires a subset of *k*-space data after each excitation, reduces these artifacts relative to conventional single-shot acquisitions. However, corrections for motion-induced phase errors are not straightforward in accelerated, diffusion-weighted multi-shot EPI because of phase aliasing. In this study, we introduce a simple acquisition and corresponding reconstruction method for diffusion-weighted multi-shot EPI with parallel imaging suitable for use at high field. The reconstruction uses a simple modification of the standard SENSE algorithm to account for shot-to-shot phase errors; the method is called Image Reconstruction using Image-space Sampling functions (IRIS). Using this approach, reconstruction from highly aliased *in vivo* image data using 2-D navigator phase information is demonstrated for human diffusion-weighted imaging studies at 7 Tesla. The final reconstructed images show submillimeter in-plane resolution with no ghosts and much reduced blurring and off-resonance artifacts.

Keywords

IRIS; DTI; SENSE; multi-shot; navigator; motion correction; 7 Tesla

INTRODUCTION

Diffusion-weighted imaging (DWI) has been widely used for investigating the microscopic motion of water in tissues (1,2). One of the main challenges in DWI, however, is to reduce the effect of subject motion while preserving the sensitivity to intravoxel incoherent motion. The two major sources of motion are: (i) non-rigid brain deformation associated with the cardiac cycle (3,4) and (ii) rigid-body head motion (5). In regard to the former issue, DWI is often synchronized to the cardiac cycle to avoid imaging during systolic phases, that results

Corresponding author: Ha-Kyu Jeong, Ph.D., Vanderbilt University Institute of Imaging Science, 1161 21st Ave South, AA 1105 Medical Center North, Nashville, TN 37232-2310., Phone: (615) 322-7149., Fax: (615) 322-0734., ha-kyu.jeong@vanderbilt.edu.

in localized nonlinear phase corruptions and signal losses (3). The result of random rigid-body motion, e.g., translation and rotation, is a linear phase shift in *image*-space which generates a constant phase error and shift of echo signal in *k*-space (5). Because diffusion-weighted (DW) images are usually acquired using strong gradients for sensitizing water molecular diffusion (6), even a small level of subject motion in the presence of the gradients can generate large phase variations between *k*-space profiles (or views) and cause significant ghost artifacts in reconstructed images unless the phase variations are properly corrected (5).

One method to avoid this problem is to acquire all echo signals after a single excitation, providing the same motion-related phase errors to all *k*-space profiles. The effect of the motion is then a spatially dependent phase error, which is discarded in reconstruction of the magnitude image. Single-shot echo-planar imaging (ssh-EPI) is capable of fast acquisition, reducing scan time and image degradation due to physiologic or involuntary subject motion (7,8). For these reasons, ssh-EPI has been very successful for both DWI and diffusion tensor imaging (DTI) (9). However, ssh-EPI is very sensitive to off-resonance effects (caused by magnetic field inhomogeneity, e.g., at air-tissue interfaces), due to its relatively small bandwidth along the phase-encoding direction. This often results in severe geometric distortions and signal losses in reconstructed images. In addition, ssh-EPI has a relatively long echo-train length compared with the transverse relaxation time. This renders ssh-EPI prone to blurring artifacts and limited spatial resolution (10). Therefore, ssh-EPI has not been a preferred choice for acquiring images at high spatial resolution.

Parallel imaging methods, especially sensitivity encoding (SENSE) (11), have dramatically improved the performance of ssh-EPI. The main benefit of parallel imaging is that it can accelerate image acquisition by increasing the acquisition bandwidth. Hence ssh-EPI combined with parallel imaging can reduce the effect of off-resonance, blurring and chemical shift artifacts while maintaining robustness to motion (12). Therefore, the combination of parallel imaging and partial Fourier acquisition has been a favored choice for DW ssh-EPI acquisitions at relatively low to medium magnetic field strength such as at 1.5 or 3 Tesla (T) (13,14). However, due to increased magnetic field inhomogeneities and reduced transverse relaxation times at ultra-high magnetic field strengths, e.g., at 7 T, even ssh-EPI with parallel imaging presents significant artifacts compared to lower magnetic field strengths. One method to reduce those artifacts is to use higher parallel acceleration to further increase the *k*-space velocity, but the signal to noise ratio (SNR) degrades at high acceleration factors (11). Other methods rely on different types of pulse sequences, each of which has its own cost. A comprehensive review of acquisition methods is given in (15).

As an alternative, multi-shot EPI (msh-EPI) acquires only a subset of *k*-space samples following each excitation. In this approach, bandwidth-related EPI artifacts can be reduced beyond the limit for conventional ssh-EPI. However, phase variations between subsets of *k*-space data, due to small shot-to-shot variations in subject motion, lead to strong ghost artifacts. Navigator-echo acquisitions can be used to retrospectively correct view-to-view motion-induced phase alterations in multi-shot acquisitions (5,16–18). Because image-echo and navigator-echo signals are both diffusion-weighted and have the same extra phase terms caused by subject motion, the phase changes between *k*-space samples of the image-echo can be corrected using the phase estimates from the navigator-echo. Several DWI methods using the navigator approach have been studied using msh-EPI (19–22) with 1-D or 2-D navigator acquisitions, as well as self-navigated approaches using spiral (23) and PROPELLER (24) sequences. Recently, multi-shot DWI approaches have been improved by combining them with parallel imaging methods (25–27) for generating DW images at relatively high spatial resolution with reduced artifacts. However, multi-shot DWI remains challenging at high field strengths because of the strong off-resonance effects, short transverse relaxation times, and limitations on SAR.

In this study, we developed an efficient reconstruction method for DW interleaved msh-EPI acquisitions with SENSE acceleration and motion-induced phase correction using a 2-D navigator implemented at 7 T for human imaging. An analytic expression is derived for the aliasing generated by multi-shot and SENSE undersampling along the same axis based on the *k*-space sampling function. It is then Fourier transformed providing an *image*-space sampling function, or point spread function (PSF). With Cartesian sampling, the aliasing is the same for each image column along the direction of undersampling (usually the phase-encoding direction), so image reconstruction can be performed by serial inversion of the encoding matrix for each image column, unlike the encoding matrix for the entire set of *k*-space data (25,28). This column-by-column reconstruction method, called Image Reconstruction using Image-space Sampling functions (IRIS), can be performed without resorting to an iterative algorithm, such as the conjugate gradient method, which is necessary when dealing with the very large matrices needed to reconstruct an entire image e.g., from non-Cartesian sampled data. Because of its column-wise *image*-space processing, it is straightforward and less computationally demanding for parallel image reconstruction. Because our multi-shot approach is built upon the conventional multi-shot sequence, it maintains the benefits of the traditional approach, i.e., less demanding on readout speed and gradient power, in addition to the aforementioned computational efficiency.

In this paper, we demonstrate that highly aliased *in vivo* DW image data, produced by multi-shot and regularly sub-sampled SENSE acquisitions, can be reconstructed with motion-induced phase correction to provide images with high spatial resolution, no residual ghosts, and much reduced susceptibility and blurring artifacts. Preliminary results from this work have been presented elsewhere (29). Recently, msh-EPI based DWI studies at 7 T (30) have also been published using GRAPPA (31), navigator based reacquisition (32), and readout-segmented EPI (26,33).

THEORY

Image aliasing due to k-space undersampling

Consider the coordinates of *k*-space k_y sampling for a multi-shot interleaved acquisition. In the case of uniform Cartesian sampling, each line in the phase-encoding direction (y) is at location

$$k_y = pn_s\Delta k + (s-1)\Delta k, \quad [1]$$

where n_s and s ($s \in \{1,2,\ldots,n_s\}$) denote the number of excitations or shots and the index of each shot, respectively. The index p denotes the echo number in the EPI echo train and Δk is the sampling interval for a fully sampled acquisition. If the trajectory is modified to take advantage of SENSE acceleration with the factor R, then Δk can be replaced by $R\Delta k$ to find the sampled spatial frequencies,

$$k_y = pn_sR\Delta k + (s-1)R\Delta k. \quad [2]$$

The corresponding *k*-space sampling function, $H(k)$, becomes

$$H(k_y) = \sum_p \delta\left(\frac{k_y - (s-1)R\Delta k}{n_sR\Delta k} - p\right). \quad [3]$$

The inverse Fourier transform of Eq.[3] is the *image*-space sampling function or PSF which is convolved with the true image to generate an aliased image due to k-space undersampling. The PSF is then

$$h(y)=e^{i2\pi a_s y}\sum_q \delta\left(y-q\frac{L}{n_s R}\right), \quad [4]$$

here $a_s \equiv (s^{-1})R\Delta k$, $L \equiv 1/\Delta k$ is the field of view (FOV), and the sum is over the index q ($q\in\{-\infty,\ldots,\infty\}$), an integer shifting the spatial position of the delta functions by multiples of L/n_sR. The leading exponential term in Eq.[4] corresponds to the Fourier shift theorem and reflects the fact that the k-space sampling function, $H(k_y)$, is shifted from shot to shot. The inverse Fourier transform from Eq.[3] to Eq.[4] is given in Appendix A. The aliased image, g, is then generated by the convolution of the PSF and the true image f,

$$\begin{aligned} g(y)&=h(y)*f(y)\\ &=\sum_q f\left(y-q\tfrac{L}{n_s R}\right)e^{iq\varphi_s}, \end{aligned} \quad [5]$$

where $\varphi_s \equiv 2\pi(s-1)/n_s$. Assuming that the phase-encoding direction lies along image columns, the aliasing is in the column direction and unfolding can be performed independently in each column. The column vector, $\mathbf{g}_j$, taken from the j^{th} column of the aliased image, is generated by folding the ideal image, $\mathbf{f}_j$, taken from the corresponding column of the unaliased image. The matrix-vector representation of Eq.[5] for the s^{th} shot becomes,

$$\mathbf{g}_{j,s}=\begin{pmatrix} \mathbf{I} & e^{i\varphi_s}\mathbf{I} & e^{i2\varphi_s}\mathbf{I} & \cdots & e^{i(n_sR-1)\varphi_s}\mathbf{I} \\ e^{-i\varphi_s}\mathbf{I} & \mathbf{I} & e^{i\varphi_s}\mathbf{I} & \cdots & e^{i(n_sR-2)\varphi_s}\mathbf{I} \\ \vdots & \vdots & \ddots & \cdots & \vdots \\ \vdots & \vdots & & \ddots & \vdots \\ e^{i(n_sR-1)\varphi_s}\mathbf{I} & e^{i(n_sR-2)\varphi_s}\mathbf{I} & \cdots & \cdots & \mathbf{I} \end{pmatrix}\mathbf{f}_j, \quad [6]$$

here $\mathbf{I}$ is the identity matrix of $N/(n_sR) \times N/(n_sR)$ elements, assuming N voxels in the ideal image along the phase-encoding direction. Note that only $N/(n_sR)$ rows in Eq.[6] are independent, since the $[N/(n_sR) + 1]^{\text{th}}$ row is equal to the 1^{st} row times $\exp(-i\varphi_s)$. Taking just the top $N/(n_sR)$ rows of Eq.[6] provides

$$\begin{aligned} \mathbf{g}_{j,s}&=\begin{pmatrix} \mathbf{I} & e^{i\varphi_s}\mathbf{I} & e^{i2\varphi_s}\mathbf{I} & \cdots & e^{i(n_sR-1)\varphi_s}\mathbf{I} \end{pmatrix}\mathbf{f}_j\\ &=\mathbf{A}_s\mathbf{f}_j. \end{aligned} \quad [7]$$

When transverse magnetization accrues an extra-phase, φ_M, due to subject motion during diffusion sensitization, the image for the s^{th} shot acquires an additional phase term. To account for the added phase, Eq.[7] becomes

$$\mathbf{g}_{j,s}=\mathbf{A}_s\mathbf{P}_{j,s}\mathbf{f}_j \quad [8]$$

where $\mathbf{P}_{j,s}$ is a diagonal matrix with non-zero elements $(P_{j,s})_{\rho\rho} = \exp[i\varphi_M(y_\rho)]$ and y_ρ is the y coordinate of the ρ^{th} image voxel in column j, with $\rho\in\{1,2,\ldots,N\}$. For multi-coil data acquisition, Eq.[8] can be written for each coil as Eq.[9] similarly as in (25,34)

$$\mathbf{g}_{j,c,s}=\mathbf{A}_s\mathbf{S}_{j,c}\mathbf{P}_{j,s}\mathbf{f}_j \quad [9]$$

where $\mathbf{S}_{j,c}$ is a diagonal matrix with diagonal elements $(S_{j,c})_{\rho\rho} = S_{j,c}(y_\rho)$ equal to the sensitivities in column j of coil c at positions y_ρ. Then the aliased image voxel for column j with the c^{th} coil sensitivity and the s^{th} interleaf can be given by,

$$g_{j,c,s}\left(y_{\rho'}\right)=\sum_q e^{iq\varphi_s}S_{j,c}\left(y_{\rho'+q\Omega}\right)P_{j,s}\left(y_{\rho'+q\Omega}\right)f_j\left(y_{\rho'+q\Omega}\right), \quad [10]$$

here $\Omega \equiv N/(n_sR)$, $\rho' \equiv \text{mo}(\rho\text{d} - 1\Omega) + 1$, $\rho' \in \{1,2,\ldots,\Omega\}$, $q \equiv [(\rho-1)-\text{mod}(\rho-1,\Omega)]/\Omega$, and $q \in \{0,1,\ldots,n_sR-1\}$. Equation [10] looks similar to that used for typical SENSE acquisitions, but here it is generalized to account for shot-to-shot phase errors due to subject motion with a new term for the shift in k-space sampling corresponding to multi-shot acquisitions combined with parallel imaging. Combining all three matrices, $\mathbf{A}_s$, $\mathbf{S}_{j,c}$ and $\mathbf{P}_{j,s}$, as the encoding matrix $\mathbf{E}_{j,c,s}$ and appending $\mathbf{g}_{j,c,s}$ and $\mathbf{E}_{j,c,s}$ in the column direction for all coils, shots and/or multiple acquisitions, Eq.[9] becomes

$$\mathbf{g}_j=\mathbf{E}_j\mathbf{f}_j. \quad [11]$$

Equation [11] shows that the true image can be reconstructed from the aliased image using a simple inversion of the encoding matrix whose elements depend on the coil sensitivity, motion-induced extra-phase terms and shifting of k-space sampling due to the interleaved acquisition. After combining all the coil sensitivities and phase errors, reconstruction of each image column can be given as Eq.[12] as in (11) without considering noise correlation

$$\widehat{\mathbf{f}}_j=\left(\mathbf{E}_j^{\text{H}}\mathbf{E}_j\right)^{-1}\mathbf{E}_j^{\text{H}}\mathbf{g}_j. \quad [12]$$

The entire image was reconstructed over all image columns considering the noise correlation matrix incorporated into Eq.[12] similarly as in (35). The geometry factor was also calculated as usual.

Differences in acquisition bandwidth and its compensation

A navigator-echo is required to generate a 2-D motion-induced phase map. Therefore, only SENSE acceleration was applied to the navigator-echo acquisitions so that the navigator image is reconstructed for each shot, whereas image-echo k-space data are acquired with SENSE and multi-shot undersampling. In this case, the image-echo and navigator-echo are acquired with different bandwidths along the phase-encoding direction due to different k-space sampling intervals. This difference in the acquisition bandwidths generates unequal susceptibility-induced geometric distortions between the image-echo and navigator-echo images (15). Because motion-induced phase terms and the true image intensities are to be multiplied voxel by voxel, a relatively large spatial mismatch can result in inaccurate image reconstruction. The amount of geometric distortion in conventional EPI with multi-shot and SENSE acceleration can be represented as the displacement in voxels (Δd), similarly to (36,37), as

$$\Delta d=\frac{\gamma}{2\pi}\frac{\Delta B_0}{\left(\frac{1}{T_s}\right)}\left(\frac{L}{n_sR\Delta y}\right), \quad [13]$$

where γ is the gyromagnetic ratio, ΔB_0 is the field-offset, and T_s is the sampling interval between adjacent k_y lines at $k_x = 0$ and Δy is the size of voxel along the phase-encoding direction. Because the same SENSE R for image- and navigator-echo acquisitions is used in this study, the navigator-echo image has n_s times the distortions present in the image-echo image. In order to apply the navigator-echo image data at the correct points in the image-echo image, the navigator data must be transformed to the image-echo image space. With the effective acquisition bandwidth (BW) in the phase-encoding direction defined as

$$BW = \frac{n_s R \Delta y}{L T_s}, \quad [14]$$

a voxel with dimensionless coordinate y_{nav} in the navigator image will appear at the location y_{img} in the image-echo image given by

$$\begin{aligned} y_{img} &= y_{nav} + \tau \left(\Delta d_{img} - \Delta d_{nav} \right) \\ &= y_{nav} + \tau \frac{\gamma}{2\pi} \Delta B_0 \left(\frac{BW_{nav} - BW_{img}}{BW_{img} BW_{nav}} \right), \end{aligned} \quad [15]$$

where τ is the polarity (±1) of the EPI phase-encoding relative to the k_y axis. Transforming the navigator image data according to Eq.[15] uses ΔB_0 measurements to warp the navigator data into the appropriate position in the image-echo image space. Use of a ΔB_0 fieldmap for the correction of susceptibility-induced geometric distortions at 7 T has been demonstrated elsewhere (38).

MATERIALS AND METHODS

Pulse sequence

A dual spin-echo DW msh-EPI pulse sequence was developed as shown in Fig. 1. The second 180 degree RF refocusing pulse was followed by the navigator-echo acquisition. In the sequence, both the image-echo and navigator-echo acquisitions were accelerated by SENSE. Only the image-echo was acquired with additional undersampling using multiple shots, as formulated in Eq.[2]. The length of the EPI echo-train was adjusted independently for each echo. For the image-echo, prephasing and postphasing gradients were applied before and after the image-echo acquisition, with variable amplitude to acquire different *k*-space interleaves in each shot and rewind back to $k_y = 0$. The navigator-echo, after the 2nd refocusing pulse, used a prephasing gradient pulse of constant amplitude to acquire the same segment of *k*-space for every shot, as in (19,26), covering the center of *k*-space and allowing navigator image reconstruction for individual shots. Echo time shifting was also applied for smooth *k*-space modulation of magnitude and phase errors (39,40).

Measurement of extra-phases from navigator

The motion-induced phase terms were measured using the navigator image. The navigator-echo *k*-space data were zero-padded to N/R lines along the phase-encoding direction and then multiplied by a *k*-space filter to reduce artifacts from truncation (24,25). A filter was also applied in the readout direction to remove high spatial frequency components equally in the two dimensions. The data were then inverse Fourier transformed, generating a complex aliased image for each coil channel, and unfolded using conventional SENSE reconstruction generating a complex navigator-echo image for each shot. The *k*-space trajectory for the navigator-echo acquisitions covered only central lines. Hence, the spatial resolution of the reconstructed navigator-echo image was much lower than the image-echo image. To compensate for the spatial misalignment between the image- and navigator-echo images due

to differences in acquisition bandwidth, the reconstructed navigator images were transformed into the image-echo *image*-space as shown in Eq.[15]. Data from the j^{th} column of the spatially aligned navigator phase map were then used to form the matrix $\mathbf{P}_{j,s}$. It was then incorporated into the encoding matrix for reconstruction of the image-echo image using Eq.[12].

In vivo data acquisition

Diffusion-weighted dual spin-echo, SENSE accelerated msh-EPI brain data were acquired from four healthy volunteers on a 7 T Philips Achieva whole body scanner (Philips Healthcare, Cleveland, USA) using the pulse sequence shown in Fig. 1 with a volume head coil for transmission and 32 channel coil array for reception (Nova Medical Inc., Wakefield, MA). Imaging parameters were: FOV 210 – 240 mm; TR 2050 – 3844 ms; TE (image-echo) 65 – 76 and TE (navigator-echo) 104 – 114 ms; SENSE factor 3; echo-train 13; diffusion gradient orientations 12 or 15; scan time 16 – 20 min. An adiabatic inversion RF pulse (SPAIR) or the slice-selective gradient reversal (SSGR) technique was used to suppress fat signals (41).

Volume coil and individual surface coil images were acquired using a 3-D spoiled gradient echo sequence. Each of the individual coil images was divided by the volume coil image for the corresponding slice to eliminate object contrast. This raw coil sensitivity map was then processed with additional smoothing using a thin-plate spline fitting for fast extrapolation and estimation of coil sensitivity (28). Noise correlations between individual coils were also calculated from a measurement during a preparation step in the acquisition of the sensitivity data and incorporated into Eq.[12] for image reconstruction. A ΔB_0 fieldmap (~ 1 to 2 min scan) was also acquired using a 3-D gradient echo sequence with ΔTE = 1 ms and TR/TE of about 5/2 ms to correct mismatches in geometric distortions between image- and navigator-echo images.

Diffusion-weighted multi-shot images were acquired and reconstructed for lower brain slices where image distortions and B_1 inhomogeneity effects are most significant (Figure 3). Single-shot and msh results were compared for DW images and maps of fractional anisotropy (FA) with directionally encoded color (DEC) of regions with small white matter fiber bundles (Figure 4). For comparison, DW ssh images were also acquired at the typical scan resolution of about 2.0 mm isotropic voxels with partial Fourier acquisition (factor 0.68) and the same SENSE factor and diffusion encoding parameters. Higher spatial-resolution DW data were also acquired of sagittal and/or coronal slice orientations for depicting DW contrast at boundaries between gray and white matter and in the hippocampus. Multiple (i.e., repeated) data acquisitions were performed and incorporated during image reconstruction as shown in the Theory section (see Figure captions for the number of averages). All image reconstruction and post-processing steps, including image co-registration using 12 parameter affine transform (42) and tensor calculation, were performed offline using Matlab (MathWorks, Natick, MA). The study protocol was approved by Vanderbilt University's institutional review board.

RESULTS

Figure 2 shows an example for motion correction using the proposed method for $b = 0$ (Fig. 2a) and 1000 s/mm^2 without (Fig. 2b) and with (Fig. 2c) correction of motion-induced phase variations for one of the 15 diffusion encoding gradients. A fractional anisotropy DEC map (Fig. 2d) and mean diffusivity (Fig. 2e) map are also shown with diffusivity scale bar in cm^2/s units. Using conventional SENSE reconstruction (with no phase correction, performed offline), the DW image (Fig. 2b) shows significant ghosting artifacts due to phase variations between excitations. However, no ghosts are visible in the DW image (Fig. 2c), FA DEC

map (Fig. 2d) and mean diffusivity map (Fig. 2e) reconstructed using IRIS. Figure 3 shows reconstructed images for $b = 0$ (a–e) and 1000 s/mm^2 (f–j) and FA DEC maps (k–o) for slices through the basal ganglia (Figs.3a,f,k) to the top of corpus callosum (Figs.3e,j,o) showing minimal distortions and blurring effects, whereas the conventional ssh approach shows significant effects at the same slice level (not shown). Figure 4 shows a comparison between ssh-EPI (Figs.4a,c,e) and proposed msh-EPI with IRIS (Figs.4b,d,f) for a DW image, FA DEC map and a magnified ROI drawn on the FA DEC map at the same slice level. As expected, the single-shot acquisition results (Figs.4a,c,e) show much larger geometric distortions and blurring artifacts than the results using IRIS (Figs.4b,d,f). The magnified ROI (Fig. 4f) shows details of small white matter fiber bundles using our approach, whereas the conventional approach (Fig. 4e), even with SENSE and partial Fourier acquisition, shows significant blurring of fiber structures. The blurring in the conventional approach cannot be reduced by averaging more acquisitions, unless the length of echo-train is reduced. Figure 5 shows high spatial resolution DW images (Figs.5a,c) and corresponding FA DEC (Figs.5b,d) maps acquired with 0.7 mm in-plane voxels in coronal and sagittal orientations, respectively. With the current approach, reconstructed DW images and FA DEC maps are presented with no significant blurring, distortion or motion-induced ghosting artifacts. The ROI in the solid red boxes in Figs.5c and 5d represents a region with cortical gray and white matter enlarged in Figs.5e and 5f. Diffusion anisotropy is clearly demonstrated for large and small white matter fibers and also cortical gray matter. Figure 6 presents a DW image with higher spatial resolution acquired for 0.8×0.92×1.5 mm^3 image voxels and $b = 700$ s/mm^2 with an ROI drawn in the left hippocampal regions (Fig. 6a) and an enlarged ROI (Fig. 6b) and corresponding FA DEC map (Fig. 6c) with color of red (right-left), green (anterior-posterior) and blue (superior-inferior). This suggests the potential for future investigation of small structures in the hippocampus, e.g., the cornu ammonis and parahippocampal gyrus, that can be delineated with DW contrast at high resolution in each of the diffusion sensitizing gradient orientations (only one example shown here).

DISCUSSION AND CONCLUSIONS

High spatial resolution DW images were successfully reconstructed using the proposed pulse sequence and reconstruction methods with reduced off-resonance and blurring artifacts and no apparent ghosting. The resulting DW images and FA maps presented clearer details in small white matter fiber bundles compared with conventional single-shot results, where larger geometric distortions and blurring artifacts were apparent due to lower bandwidth and greater echo-train length, even using SENSE and partial Fourier acquisition. Good delineation between gray and white matter was presented near cortical regions in DW images and FA DEC maps. The regional variations of directionally encoded FA values in cortical gray matter in high spatial resolution suggests variations in cellular size and organization in these regions, as observed in other studies (43,44). The hippocampus was visualized at high spatial resolution with DW contrast so that different hippocampal regions, e.g., dentate gyrus, cornu ammonis, subiculum and parahippocampal gyrus, were clearly delineated as shown in a postmortem DTI study of the human hippocampus (45). Overall, this study suggests that IRIS is well suited for investigating small brain structures with high spatial resolution at 7 T.

For investigating fine structures in the brain using DTI, it is important to guarantee that the effects of eddy-currents generated by strong diffusion gradients are effectively compensated. Because eddy-currents can impose additional distortions in DW images based on the direction of applied diffusion sensitization, rimming and blurring artifacts can be usually observed in anisotropy maps for pixels close to boundaries of different tissue types (46). In this study, image co-registration between non-DW and DW images are used as corrections.

The effect of eddy-currents is then properly compensated, where no significant rimming and blurring artifacts are observed in the FA DEC maps.

A mathematical framework for sampling and reconstruction of DW SENSE accelerated msh-EPI data has been derived using the *k*-space sampling function and its reciprocal, the *image*-space PSF. A conventional dual spin-echo pulse sequence was also implemented with 2-D navigation, multi-shot and SENSE acceleration combined for further reduction of off-resonance and blurring artifacts, the main concern when ssh-EPI is used for high spatial resolution imaging. While our approach is capable of generating DW images with quality superior to ssh-EPI at 7 T, remaining artifacts, e.g., signal dropout and distortions, can be observed in some regions of brain, e.g., orbitofrontal cortex, as shown in Figs. 5c and 5d. However, these artifacts are also strongly dependent on subject and other scan parameters, e.g., size of sinuses and shimming conditions.

There are several benefits to our approach. First, most modern MRI scanners have well-optimized conventional EPI sequences. Our pulse sequence can be developed from existing multi-shot or single-shot EPI sequences. Because msh-EPI is usually less demanding of gradient performance and measurement speed in general, it is also suited for clinical scanners with relatively low performance gradient coils (47). The use of msh-EPI, however, must be considered as a trade-off between EPI-related artifacts and total scan time. Next, our approach uses coherent aliasing of image voxels in the column direction due to uniform *k*-space undersampling using multi-shot and SENSE acceleration, so that each image column can be independently unfolded without requiring information from adjacent image columns. This is not the case in non-uniform sampling where *k*-space undersampling appears as an incoherent artifact rather than the aliasing of image voxels along the undersampling direction. However, this randomness in *k*-space undersampling has been used in non-linear image reconstruction (48). Our reconstruction algorithm takes advantage of the simple structure of ghosts in undersampled Cartesian acquisitions, at the expense of the flexibility provided by non-Cartesian sampling trajectories.

There is virtually no limitation on the number of shots or the type of navigator trajectory in our method, assuming a reliable navigator-echo image can be reconstructed. For example, a spiral navigator-echo with echo-planar image-echo readout could be combined as in (22). Lastly, the proposed method provides relatively simple multi-shot and multi-coil image reconstruction with motion-induced phase correction. In this approach, the phase correction is implemented in *image*-space, where nonlinear phase correction is straightforward. Motion correction performed directly in *k*-space is more limited and usually requires regridding for 2-D linear phase correction with higher order phase variations posing a greater challenge. Although the image-space column-wise reconstruction can be performed by a single inversion of the encoding matrix, it is somewhat more computationally demanding than typical SENSE reconstruction. However, most components building the encoding matrix, i.e., **A**, **S** and/or the noise correlation matrix, can be precalculated prior to the actual DWI scan. In this case, DW image reconstruction using the final encoding matrix including **A**, **S**, **P** and/or the noise correlation matrix may be performed efficiently, provided that low resolution 2-D navigator images necessary in forming **P** are reconstructed without significant delay. The reconstruction speed will depend on the computing power and size of the encoding matrix which reflects image resolution, number of shots, number of coils, number of averages and SENSE factor.

The notion of image column-by-column reconstruction has been used previously in the *hybrid*-space, where the choice of phase-encoding scheme results in significant variations in the quality of the reconstructed image (46). In IRIS, a prescribed phase-encoding scheme is

used as formulated in the PSF, and image reconstruction has been performed in the *image*-space with consideration of noise correlation and motion-induced phase correction.

Compensation for spatial misalignment between image- and navigator-echoes has been obtained using a measured fieldmap and known acquisition bandwidth for each echo. Though it is possible that there is only a linear phase error in *image*-space due to rigid-body motion of a subject, the linear phase error can appear as nonlinear phase distributions due to local susceptibility-induced geometric distortions (49). Then it is important to make sure that image- and navigator-echo images are in co-registration for accurate motion-induced phase correction. Direct image co-registration has also been used for this purpose at 3 T (34). If the navigator *k*-space trajectory can be designed to have the same acquisition bandwidth as the image-echo, separate fieldmap acquisition is not necessary for spatial alignment between image- and navigator-echo images.

In this study, we presented DW images with submillimeter in-plane and relatively small slice thickness resulting in 1.1 to 3.6 mm^3 image voxels. The overall image SNR and quality of reconstructed images were limited by B_1 inhomogeneity at 7 T. This can generate strong variations of SNR over the brain as shown in Figs.3, 5 and 6. The SNR drop is more significant in the acquisition of the navigator-echo signal due to incomplete refocusing of the slice (i.e., nonideal slice profile) and longer echo time. Hence, a requirement of the method is that the overall SNR for each acquisition is maintained so the navigator image, including regions with low B_1 homogeneity, could be reconstructed with SENSE for each shot. With the experimental set up used in this study, the navigator-echo data were reconstructed with fair SNR and used for the final DW image reconstruction with phase correction by combining 3 or 5 acquisitions. If a DW image was reconstructed without phase correction, it showed significant ghosting artifacts, regardless of whether single (not shown) or repeated acquisition (Fig. 2b) was used. Provided that the phase correction was implemented, multiple acquisitions were also required for better matrix conditioning and image SNR. The rationale for multiple acquisitions in the motion correction of DW multi-shot data is well stated in (19) in which the repeated measures allow the Nyquist criterion to be met in image reconstruction. Using larger slice thickness for refocusing can improve the slice profile and, hence, increased SNR may be achieved, as was shown with DW radial fast spin-echo acquisitions at 3 T (50).

The range of our navigator *k*-space trajectory along the phase-encoding direction was 17 k_y lines around the center of *k*-space. However, with a SENSE acceleration factor of 3, the effective *k*-space coverage of the acquisition is $17/(L/3) = \pm 25.5\Delta k$ along the k_y direction with full k_x coverage. This navigator acquisition range may be enough to cover most of the *k*-space shift caused by small to moderate subject motion. However, for relatively large phase errors, the navigator based rejection and reacquisition scheme, based on a threshold of peak navigator signal intensity and broadening of the signal, will be useful for more robust motion-induced phase correction (19,32). Recently, this scheme has been applied to 7 T human DW multi-shot imaging using GRAPPA accelerated readout-segmented EPI (30).

Acknowledgments

This work has been supported by NIH Bioengineering Research Partnership (BRP) grant (RO1 EB000461).

LIST OF SYMBOLS

Δ	Upper case Greek delta
k	Italic k

p	Italic p
s	Italic s
n_s	Italic n, subscript *s*
a_s	Italic a, subscript *s*
L	Upper case italic L
φ_s	Greek phi, subscript *s*
b_s	Italic b, subscript *s*
R	Italic R
$\mathbf{g}_{j,\,c,s}$	Lower case bold g, subscripts '*j,c,s*'
$g_{j,\,c,s}$	Lower case g, subscripts '*j,c,s*'
$\mathbf{I}$	Bold I
$\mathbf{f}_j$	Lower case bold f, subscript *j*
f_j	Lower case italic f, subscript *j*
$\mathbf{A}_s$	Upper case bold A, subscript *s*
$\mathbf{P}_{j,s}$	Upper case bold P, subscripts '*j,s*'
$\mathbf{S}_{j,c}$	Upper case bold S, subscripts '*j,c*'
$\mathbf{E}_{j,\,c,s}$	Upper case bold E, subscripts '*j,c,s*'
$P_{j,s}$	Upper case italic P, subscripts '*j,s*'
$S_{j,c}$	Upper case italic S, subscripts '*j,c*'
$E_{j,c,s}$	Upper case italic E, subscripts '*j,c,s*'
Ω	Upper case Greek omega
ρ	Lower case Greek rho
ρ'	Lower case Greek rho, superscript ′
$\hat{\mathbf{f}}_j$	Lower case bold f caret, subscript *j*
Ψ	Upper case bold Greek psi
Φ	Upper case bold Greek phi
α	Lower case Greek alpha
T_s	Upper case italic T, subscript *s*
γ	Lower case Greek gamma
ε	Lower case Greek epsilon

References

1. Le Bihan D, Breton E, Lallemand D, Grenier P, Cabanis E, Laval-Jeantet M. MR Imaging of Intravoxel Incoherent Motions: Application to Diffusion and Perfusion in Neurologic Disorders. Radiology. 1986; 161:401–407. [PubMed: 3763909]
2. Moseley ME, Cohen Y, Kucharczyk J, Mintorovitch J, Asgari HS, Wendland MF, Tsuruda J, Norman D. Diffusion-weighted MR imaging of anisotropic water diffusion in cat central nervous system. Radiology. 1990; 176:439–445. [PubMed: 2367658]

3. Miller KL, Pauly JM. Nonlinear phase correction for navigated diffusion imaging. Magn Reson Med. 2003; 50:343–353. [PubMed: 12876711]
4. Poncelet BP, Wedeen VJ, Weisskoff RM, Cohen MS. Brain parenchyma motion: measurement with cine echo-planar MR imaging. Radiology. 1992; 185:645–651. [PubMed: 1438740]
5. Anderson AW, Gore JC. Analysis and correction of motion artifacts in diffusion weighted imaging. Magn Reson Med. 1994; 32:379–387. [PubMed: 7984070]
6. Stejskal EO, Tanner JE. Spin Diffusion Measurements: Spin Echoes in the Presence of a Time-Dependent Field Gradient. J Chem Phys. 1965; 42:288–292.
7. Ehman RL, McNamara MT, Brasch RC, Felmlee JP, Gray JE, Higgins CB. Influence of physiologic motion on the appearance of tissue in MR images. Radiology. 1986; 159:777–782. [PubMed: 3704156]
8. Turner R, Le Bihan D. Single-shot diffusion imaging at 2.0 tesla. J Magn Reson. 1990; 86:445–452.
9. Basser PJ, Mattiello J, LeBihan D. Estimation of the effective self-diffusion tensor from the NMR spin echo. J Magn Reson B. 1994; 103:247–254. [PubMed: 8019776]
10. Farzaneh F, Riederer SJ, Pelc NJ. Analysis of T2 limitations and off-resonance effects on spatial resolution and artifacts in echo-planar imaging. Magn Reson Med. 1990; 14:123–139. [PubMed: 2352469]
11. Pruessmann KP, Weiger M, Scheidegger MB, Boesiger P. SENSE: sensitivity encoding for fast MRI. Magn Reson Med. 1999; 42:952–962. [PubMed: 10542355]
12. Bammer R, Keeling SL, Augustin M, Pruessmann KP, Wolf R, Stollberger R, Hartung HP, Fazekas F. Improved diffusion-weighted single-shot echo-planar imaging (EPI) in stroke using sensitivity encoding (SENSE). Magn Reson Med. 2001; 46:548–554. [PubMed: 11550248]
13. Bammer R, Auer M, Keeling SL, Augustin M, Stables LA, Prokesch RW, Stollberger R, Moseley ME, Fazekas F. Diffusion tensor imaging using single-shot SENSE-EPI. Magn Reson Med. 2002; 48:128–136. [PubMed: 12111940]
14. Jaermann T, Crelier G, Pruessmann KP, Golay X, Netsch T, van Muiswinkel AM, Mori S, van Zijl PC, Valavanis A, Kollias S, Boesiger P. SENSE-DTI at 3 T. Magn Reson Med. 2004; 51:230–236. [PubMed: 14755645]
15. Bammer R, Holdsworth SJ, Veldhuis WB, Skare ST. New methods in diffusion-weighted and diffusion tensor imaging. Magn Reson Imaging Clin N Am. 2009; 17:175–204. [PubMed: 19406353]
16. de Crespigny AJ, Marks MP, Enzmann DR, Moseley ME. Navigated diffusion imaging of normal and ischemic human brain. Magn Reson Med. 1995; 33:720–728. [PubMed: 7596277]
17. Ehman RL, Felmlee JP. Adaptive technique for high-definition MR imaging of moving structures. Radiology. 1989; 173:255–263. [PubMed: 2781017]
18. Ordidge RJ, Helpern JA, Qing ZX, Knight RA, Nagesh V. Correction of motional artifacts in diffusion-weighted MR images using navigator echoes. Magn Reson Imaging. 1994; 12:455–460. [PubMed: 8007775]
19. Atkinson D, Porter DA, Hill DL, Calamante F, Connelly A. Sampling and reconstruction effects due to motion in diffusion-weighted interleaved echo planar imaging. Magn Reson Med. 2000; 44:101–109. [PubMed: 10893527]
20. Bammer R, Stollberger R, Augustin M, Simbrunner J, Offenbacher H, Kooijman H, Ropele S, Kapeller P, Wach P, Ebner F, Fazekas F. Diffusion-weighted imaging with navigated interleaved echo-planar imaging and a conventional gradient system. Radiology. 1999; 211:799–806. [PubMed: 10352609]
21. Butts K, de Crespigny A, Pauly JM, Moseley M. Diffusion-weighted interleaved echo-planar imaging with a pair of orthogonal navigator echoes. Magn Reson Med. 1996; 35:763–770. [PubMed: 8722828]
22. Butts K, Pauly J, de Crespigny A, Moseley M. Isotropic diffusion-weighted and spiral-navigated interleaved EPI for routine imaging of acute stroke. Magn Reson Med. 1997; 38:741–749. [PubMed: 9358448]
23. Liu C, Bammer R, Kim DH, Moseley ME. Self-navigated interleaved spiral (SNAILS): application to high-resolution diffusion tensor imaging. Magn Reson Med. 2004; 52:1388–1396. [PubMed: 15562493]

24. Pipe JG, Farthing VG, Forbes KP. Multishot diffusion-weighted FSE using PROPELLER MRI. Magn Reson Med. 2002; 47:42–52. [PubMed: 11754441]
25. Liu C, Moseley ME, Bammer R. Simultaneous phase correction and SENSE reconstruction for navigated multi-shot DWI with non-cartesian k-space sampling. Magn Reson Med. 2005; 54:1412–1422. [PubMed: 16276497]
26. Porter, DA.; Heidemann, RM. Multi-Shot, Diffusion-Weighted Imaging at 3T using Readout-Segmented EPI and GRAPPA. Proceedings of the 14th Annual Meeting of ISMRM; Seattle. 2006.
27. Van AT, Karampinos DC, Georgiadis JG, Sutton BP. K-space and image-space combination for motion-induced phase-error correction in self-navigated multicoil multishot DWI. IEEE Trans Med Imaging. 2009; 28:1770–1780. [PubMed: 19884065]
28. Liu C, Bammer R, Moseley ME. Parallel imaging reconstruction for arbitrary trajectories using k-space sparse matrices (kSPA). Magn Reson Med. 2007; 58:1171–1181. [PubMed: 17969012]
29. Jeong, HK.; Anderson, AW.; Gore, JC. Multi-Shot SENSE DWI at 7T. Proceedings of the 18th Annual Meeting of ISMRM; Stockholm. 2010. p. 1616
30. Heidemann RM, Porter DA, Anwander A, Feiweier T, Heberlein K, Knosche TR, Turner R. Diffusion imaging in humans at 7T using readout-segmented EPI and GRAPPA. Magn Reson Med. 2010; 64:9–14. [PubMed: 20577977]
31. Griswold MA, Jakob PM, Heidemann RM, Nittka M, Jellus V, Wang J, Kiefer B, Haase A. Generalized autocalibrating partially parallel acquisitions (GRAPPA). Magn Reson Med. 2002; 47:1202–1210. [PubMed: 12111967]
32. Porter DA, Heidemann RM. High resolution diffusion-weighted imaging using readout-segmented echo-planar imaging, parallel imaging and a two-dimensional navigator-based reacquisition. Magn Reson Med. 2009; 62:468–475. [PubMed: 19449372]
33. Holdsworth SJ, Skare S, Newbould RD, Bammer R. Robust GRAPPA-accelerated diffusion-weighted readout-segmented (RS)-EPI. Magn Reson Med. 2009; 62:1629–1640. [PubMed: 19859974]
34. Atkinson D, Counsell S, Hajnal JV, Batchelor PG, Hill DL, Larkman DJ. Nonlinear phase correction of navigated multi-coil diffusion images. Magn Reson Med. 2006; 56:1135–1139. [PubMed: 16986111]
35. Pruessmann KP, Weiger M, Bornert P, Boesiger P. Advances in sensitivity encoding with arbitrary k-space trajectories. Magn Reson Med. 2001; 46:638–651. [PubMed: 11590639]
36. Jezzard P, Balaban RS. Correction for geometric distortion in echo planar images from B0 field variations. Magn Reson Med. 1995; 34:65–73. [PubMed: 7674900]
37. Skare S, Newbould RD, Clayton DB, Bammer R. Propeller EPI in the other direction. Magn Reson Med. 2006; 55:1298–1307. [PubMed: 16676335]
38. Jeong, HK.; Anderson, AW. High angular resolution diffusion imaging with B0 distortion correction at 7T. Proceedings of the 16th Annual Meeting of ISMRM; Toronto. 2008. p. 1811
39. Butts K, Riederer SJ, Ehman RL, Thompson RM, Jack CR. Interleaved echo planar imaging on a standard MRI system. Magn Reson Med. 1994; 31:67–72. [PubMed: 8121272]
40. Feinberg DA, Oshio K. Phase errors in multi-shot echo planar imaging. Magn Reson Med. 1994; 32:535–539. [PubMed: 7997122]
41. Volk A, Tiffon B, Mispelter J, Lhoste JM. Chemical shift-specific slice selection. A new method for chemical shift imaging at high magnetic field. J Magn Reson. 1987; 71:168–174.
42. Nunes RG, Drobnjak I, Clare S, Jezzard P, Jenkinson M. Performance of single spin-echo and doubly refocused diffusion-weighted sequences in the presence of eddy current fields with multiple components. Magn Reson Imaging. 2011; 29:659–667. [PubMed: 21531107]
43. Bhagat YA, Beaulieu C. Diffusion anisotropy in subcortical white matter and cortical gray matter: changes with aging and the role of CSF-suppression. J Magn Reson Imaging. 2004; 20:216–227. [PubMed: 15269946]
44. Anwander, A.; Pampel, A.; Knosche, TR. In vivo measurement of cortical anisotropy by diffusion-weighted imaging correlates with cortex type. Proceedings of the 18th Annual Meeting of ISMRM; Stockholm. 2010. p. 109

45. Shepherd TM, Ozarslan E, Yachnis AT, King MA, Blackband SJ. Diffusion tensor microscopy indicates the cytoarchitectural basis for diffusion anisotropy in the human hippocampus. AJNR American journal of neuroradiology. 2007; 28:958–964. [PubMed: 17494678]

46. Jezzard P, Barnett AS, Pierpaoli C. Characterization of and correction for eddy current artifacts in echo planar diffusion imaging. Magn Reson Med. 1998; 39:801–812. [PubMed: 9581612]

47. Bammer R. Basic principles of diffusion-weighted imaging. Eur J Radiol. 2003; 45:169–184. [PubMed: 12595101]

48. Lustig, M.; Lee, JH.; Donoho, DL.; Pauly, JM. Faster imaging with randomly perturbed, under-sampled spirals and l1 reconstruction. Proceedings of the 13th Annual Meeting of ISMRM; Miami Beach. 2005. p. 685

49. Storey P, Frigo FJ, Hinks RS, Mock BJ, Collick BD, Baker N, Marmurek J, Graham SJ. Partial k-space reconstruction in single-shot diffusion-weighted echo-planar imaging. Magn Reson Med. 2007; 57:614–619. [PubMed: 17326165]

50. Sarlls JE, Pierpaoli C. Diffusion-weighted radial fast spin-echo for high-resolution diffusion tensor imaging at 3T. Magn Reson Med. 2008; 60:270–276. [PubMed: 18666119]

51. Bracewell, R. The Fourier Transform and Its Applications. 2. New York, NY: McGraw-Hill; 1986. p. 214

APPENDIX A

Inverse Fourier transform of k-space sampling function

The inverse Fourier transform of Eq.[3] can be performed by noting that if $f(y)$ and $F(k_y)$ are a Fourier transform pair,

$$F\left(k_y\right) \iff f(y), \quad \text{[A1]}$$

then

$$F\left(\frac{k_y - a_s}{b}\right) \iff b f(by) e^{i2\pi a_s y}, \quad \text{[A2]}$$

using the Fourier shift and scaling theorems. Applied to the sampling function transform pair (51),

$$\sum_{p=-\infty}^{\infty} \delta\left(k_y - p\right) \iff \sum_{q=-\infty}^{\infty} \delta(y - q)$$

Eq.[A2] implies

$$\begin{aligned} \sum_p \delta\left(\frac{k_y - a_s}{n_s R \Delta k} - p\right) &\iff n_s R \Delta k \sum_q \delta(n_s R \Delta k y - q) e^{i2\pi a_s y} \\ &\iff \sum_q \delta\left(y - \frac{q}{n_s R \Delta k}\right) e^{i2\pi a_s y} \\ &\iff \sum_q \delta\left(y - q\frac{L}{n_s R}\right) e^{i2\pi a_s y}, \end{aligned} \quad \text{[A3]}$$

using the scaling property of the delta function.

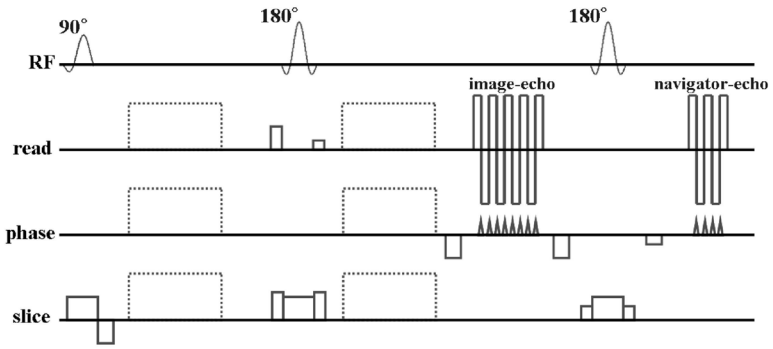

Figure 1.
A dual spin-echo DW SENSE accelerated msh-EPI pulse sequence diagram. The image-echo is followed by the navigator-echo with 180 degree RF refocusing pulse between the two echoes. Dotted lines represent diffusion gradients.

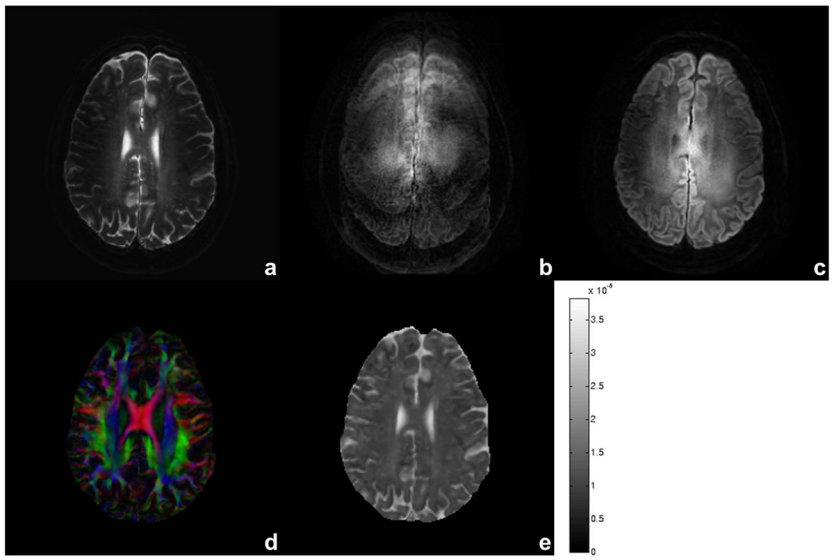

Figure 2.

Reconstructed images from for $b = 0$ (a), 1000 s/mm^2 without (b) and with (c) motion-induced phase correction using the 2-D navigator, FA DEC map (d) and mean diffusivity map (e) with intensity scale bar in cm^2/s units. Acquisition voxel size is 0.99/1.03/3.0 mm in readout/phase/slice direction with TE of 76 ms, six shots and three averages. Diffusion encoding gradient (in b and c) is close to the slice direction. Total scan time is 18 min and 39 s.

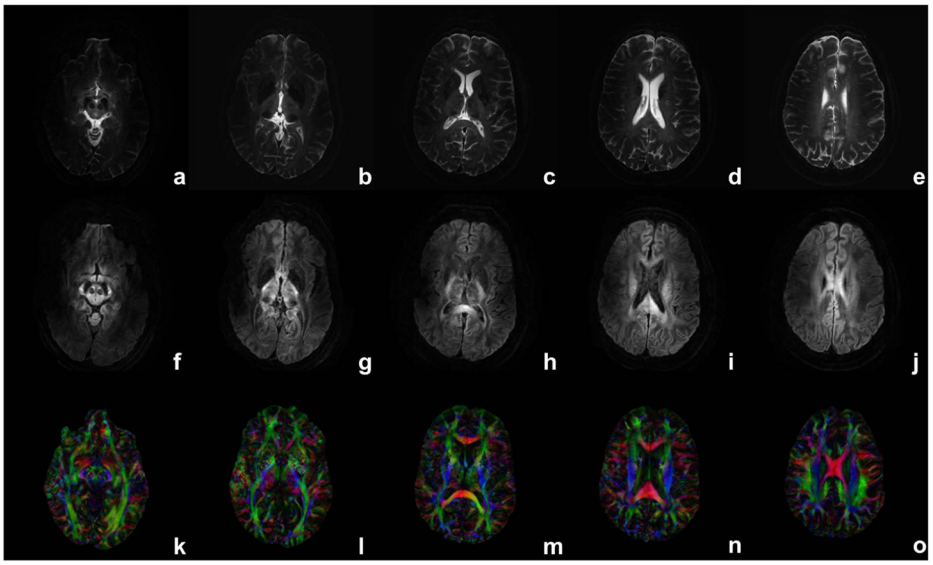

Figure 3.
Reconstructed images for $b = 0$ (a–e), 1000 s/mm^2 (f–j) and FA DEC maps (k–o) using 15 diffusion gradients over different slices. Identical scan parameters are used as in Fig. 2. Diffusion encoding gradient (in f–j) is close to the image column direction.

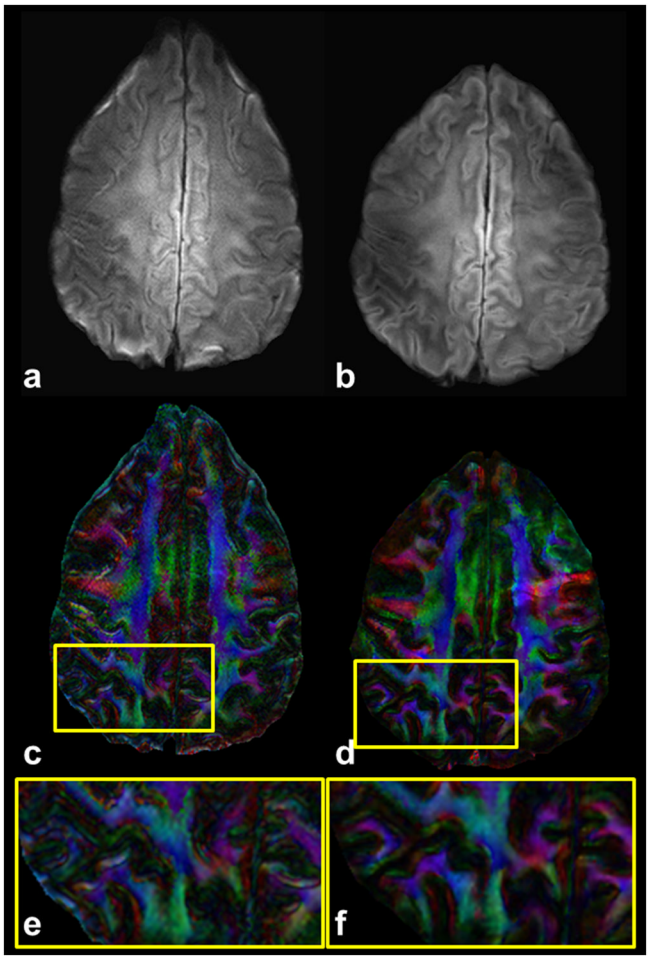

Figure 4.
Diffusion-weighted images (a,b) (b = 700 s/mm^2) and corresponding FA DEC maps (c,d) are presented with magnified ROIs (e,f) drawn in the FA DEC maps for single-shot (a,c,e) and the proposed multi-shot (b,d,f) approach. Acquisition voxel size for multi-shot data is 0.8/0.9/5.0 mm with TE of 73 ms, seven shots and two (ssh) and three (msh) averages with 15 directions. Total scan time for the multi-shot acquisition is 16 min and 16 s and single-shot is 5 min 20 s.

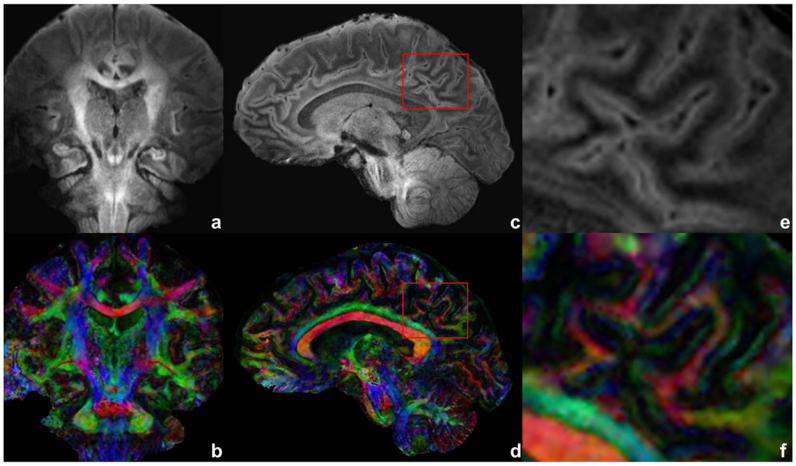

Figure 5.
Diffusion-weighted image of a coronal and sagittal slices (a,c) with $b = 700$ s/mm^2 and corresponding FA DEC maps (b,d). Acquisition voxel size is 0.7/0.72/3.0 mm with TE of 70 ms, eight shots and five averages. An ROI is drawn over the mixed region of gray and white matter as a red box in (c) and (d). The ROI is shown enlarged in (e) and (f). Total scan time is 19 min for each of coronal and sagittal acquisitions.

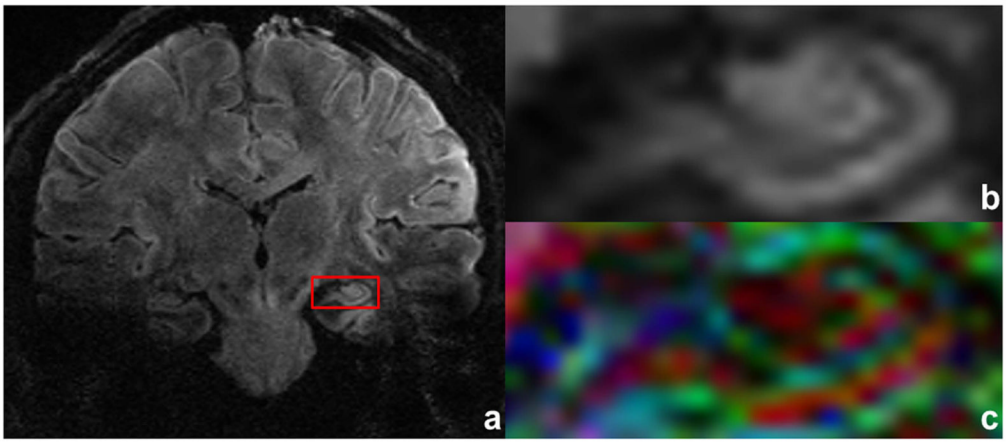

Figure 6.

Reconstructed DW image is shown in (a) acquired with $b = 700$ s/mm^2, acquisition voxel size of 0.8/0.92/1.5 mm, TE of 65 ms, six shots and five averages. An ROI is drawn in red (a), and its magnification (b) and FA DEC map (c) are provided for subject's left hippocampal regions. Total scan time is 18 min and 31 s.